AIAA '89

AIAA 89-0114
A Comparative Study of Iterative Algorithms for the Euler Equations of Gas Dynamics

D. Dorney and G. Dulikravich, Pennsylvania State Univ., Univ. Park, PA;
K. Lee, University of Illinois, Urbana, IL

27th Aerospace Sciences Meeting
January 9–12, 1989/Reno, Nevada

A COMPARATIVE STUDY OF ITERATIVE ALGORITHMS FOR THE EULER EQUATIONS OF GASDYNAMICS

Daniel J. Dorney* and George S. Dulikravich**
Department of Aerospace Engineering
The Pennsylvania State University
University Park, PA 16802
and
Ki D. Lee**
University of Illinois
Urbana, IL 61801

ABSTRACT

A comparative study for the solution of the Euler equations has been performed using four Flux-Vector-Splitting (FVS) schemes and a central difference scheme with two different dissipation models. All schemes were tested for the case of steady, inviscid, transonic airfoil flow. Van Leer's FVS scheme was found to be robust and appears to generate little numerical dissipation. The FVS schemes of Deese and Steger-Warming yield results similar to Van Leer's, though not quite as robust. Whitfield's FVS scheme generates large amounts of numerical dissipation and causes delayed post-shock pressure recovery. A new, Physically Based Dissipation (PBD) model for central difference schemes has been compared to Jameson's Artificial Dissipation (AD) model.

INTRODUCTION

Central difference numerical schemes and various forms of Flux-Vector-Splitting (FVS) schemes have received considerable attention during the last decade. Upwind (FVS) schemes are believed to be more robust than central difference schemes. In particular, they are capable of computing stronger shocks and high gradient regions where central difference schemes experience difficulties. Although upwind schemes do not require the explicit addition of dissipation terms, they still may generate significant amounts of dissipation. In addition, most FVS schemes require large amounts of computer time.

In the first part of this study the two-dimensional Euler equations of gas dynamics are presented in Cartesian and transformed coordinates. In the second part of this study the FVS schemes of following five authors are investigated: Deese [1,2], Whitfield [3], Steger and Warming [4], and Van Leer et al [5]. After describing the methods, a discussion of the numerical dissipation associated with the FVS schemes is presented.

Next, the finite volume rational Runge-Kutta central difference scheme of Jameson et al [6] is presented including a discussion of the existing Artificial Dissipation (AD) model [6]. In an effort to accurately model the physics of the flow, a Physically Based Dissipation (PBD) model was developed and compared to the AD model.

The boundary conditions can play a significant role in the generation of numerical dissipation. A discussion of solid wall and far-field boundary conditions is included.

GOVERNING SYSTEM OF EQUATIONS

The two-dimensional Euler equations of inviscid gasdynamics in conservative form and Cartesian coordinates (x,y) can be written as:

$$\frac{\partial Q}{\partial t} + \frac{\partial E}{\partial x} + \frac{\partial F}{\partial y} = 0 \tag{1}$$

where

$$Q = \begin{bmatrix} \rho \\ \rho u \\ \rho v \\ \rho e_o \end{bmatrix} \quad E = \begin{bmatrix} \rho u \\ \rho u^2 + p \\ \rho uv \\ \rho u h_o \end{bmatrix} \quad F = \begin{bmatrix} \rho v \\ \rho uv \\ \rho v^2 + p \\ \rho v h_o \end{bmatrix} \tag{2}$$

with ρ, p, u, v, e_o, h_o as the density, thermodynamic pressure, x-component of velocity, y-component of velocity, total mass-specific energy and total mass-specific enthalpy, respectively. The equation of state for a calorically perfect gas is:

$$p = (\gamma - 1)\left\{\rho e_o - \frac{1}{2}\left[\frac{(\rho u)^2}{\rho} + \frac{(\rho v)^2}{\rho}\right]\right\} \tag{3}$$

where γ is the specific heat ratio. The total mass-specific enthalpy h_o is:

$$h_o = e_o + \frac{p}{\rho} = e + \frac{1}{2}(u^2 + v^2) + \frac{p}{\rho} \tag{4}$$

where e is the mass-specific internal energy. In non-conservative form, the Euler equations are:

$$\frac{\partial Q}{\partial t} + A\frac{\partial Q}{\partial x} + B\frac{\partial Q}{\partial y} = 0 \tag{5}$$

where

$$A = \frac{\partial E}{\partial Q} \qquad B = \frac{\partial F}{\partial Q} \tag{6}$$

are the Jacobian matrices. The eigenvalues of the matrix A are:

---

* Graduate Research Assistant.
** Associate Professor.

$$\lambda_1 = \lambda_2 = u \qquad \lambda_3 = u + a \qquad \lambda_4 = u - a \tag{7}$$

where the speed of sound, a is given by:

$$a = \sqrt{\frac{\gamma p}{\rho}} \tag{8}$$

Similariy, the eigenvalues of the matrix B are:

$$\sigma_1 = \sigma_2 = v \qquad \sigma_3 = v + a \qquad \sigma_4 = v - a \tag{9}$$

For the analysis of arbitrary geometries, the formulations can be generalized by using body-fitted coordinates. Using the transformations:

$$\xi = \xi(x,y) \qquad \eta = \eta(x,y) \qquad \tau = t \tag{10}$$

the body-fitted coordinates in the physical domain become Cartesian coordinates in the computational domain. In the transformed (computational) domain, the two-dimensional Euler equations in conservative form can be written as:

$$\frac{\partial \bar{Q}}{\partial t} + \frac{\partial \bar{E}}{\partial \xi} + \frac{\partial \bar{F}}{\partial \eta} = 0 \tag{11}$$

where

$$\bar{Q} = QD \qquad \bar{E} = Ey_\eta - Fx_\eta \qquad \bar{F} = Fx_\xi - Ey_\xi \tag{12}$$

$$D = x_\xi y_\eta - x_\eta y_\xi \qquad x_\xi = \frac{\partial x}{\partial \xi} \text{ etc.}$$

In this formulation, the prime variables are defined at the cell centers, while the fluxes are defined at the cell boundaries. The fluxes may also be written as:

$$\bar{E} = \begin{bmatrix} \rho UD \\ \rho UDu + py_\eta \\ \rho UDv - px_\eta \\ \rho UDh_o \end{bmatrix} \qquad \bar{F} = \begin{bmatrix} \rho VD \\ \rho VDu - py_\xi \\ \rho VDv + px_\xi \\ \rho VDh_o \end{bmatrix} \tag{13}$$

where

$$U = (uy_\eta - vx_\eta)/D \qquad V = (-uy_\xi + ux_\xi)/D \tag{14}$$

are the contravariant velocity components normal to the gridlines. The non-conservative formulation of the transformed equations is:

$$D\frac{\partial Q}{\partial t} + \bar{A}\frac{\partial Q}{\partial \xi} + \bar{B}\frac{\partial Q}{\partial \eta} = 0 \tag{15}$$

where

$$\bar{A} = \frac{\partial \bar{E}}{\partial Q} = Ay_\eta - Bx_\eta \qquad \bar{B} = \frac{\partial \bar{F}}{\partial Q} = -Ay_\xi + Bx_\xi \tag{16}$$

Here, A and B are the Jacobian matrices written in Cartesian coordinates. The eigenvalues of the matrix A in the transformed plane are:

$$\tilde{\lambda}_1 = \tilde{\lambda}_2 = U \qquad \tilde{\lambda}_3 = U + a_\xi \qquad \tilde{\lambda}_4 = U - a_\xi \tag{17}$$

where

$$a_\xi = a\,|\nabla\xi| = a\sqrt{(x_\eta^2 + y_\eta^2)/D} \tag{18}$$

The eigenvalues of the matrix B are:

$$\tilde{\sigma}_1 = \tilde{\sigma}_2 = V \qquad \tilde{\sigma}_3 = V + a_\eta \qquad \tilde{\sigma}_4 = V - a_\eta \tag{19}$$

where

$$a_\eta = a\,|\nabla\eta| = a\sqrt{(x_\xi^2 + y_\xi^2)/D} \tag{20}$$

FLUX-VECTOR-SPLITTING

The basic concept behind Flux-Vector-Splitting [3] is to use the information from eigenvalue analysis to determine the direction from which information is extrapolated in an upwind scheme. This allows the development of valid solutions in both subsonic and supersonic regions without violating the consistency or stability of the numerical scheme. Flux-vector-splitting in two dimensions is achieved by splitting the spatial components separately, as if they represent two one-dimensional problems.

DEESE AND WHITFIELD SPLITTING

In the methods developed by Deese and Whitfield [1,2,3], the flux vectors in Eq. 13 are split into parts corresponding to the individual eigenvalues. Each part is calculated separately according to the sign of the corresponding eigenvalue. For example, the E flux in the transformed domain can be expressed as:

$$\bar{E}_1 = \tilde{\lambda}_1 \frac{\gamma - 1}{\gamma}\left(\rho, \rho u, \rho v, \rho\left(\frac{u^2 + v^2}{2}\right)\right)^* \tag{21}$$

$$\bar{E}_2 = \frac{\tilde{\lambda}_3}{2\gamma}\left(\rho, \rho u + \rho a\frac{y_\eta}{s_\eta}, \rho v - \rho a\frac{x_\eta}{s_\eta}, h_o + \rho a\frac{uy_\eta - vx_\eta}{s_\eta}\right)^* \tag{22}$$

$$\bar{E}_3 = \frac{\tilde{\lambda}_4}{2\gamma}\left(\rho, \rho u - \rho a\frac{y_\eta}{s_\eta}, \rho v + \rho a\frac{x_\eta}{s_\eta}, h_o - \rho a\frac{uy_\eta - vx_\eta}{s_\eta}\right)^* \tag{23}$$

where the superscript * denotes the transpose of a vector and

$$s_\xi = \sqrt{x_\xi^2 + y_\xi^2} \qquad s_\eta = \sqrt{x_\eta^2 + y_\eta^2} \qquad \tilde{\lambda}_1 = \tilde{\lambda}_2 \tag{24}$$

Similar relations can be defined for the F flux. When the flow variables in Eq. 21-24 are defined at cell centers, the fluxes must be evaluated at the cell boundaries. To evaluate the fluxes, a knowledge of the eigenvalues at the cell boundaries is required.

The method suggested by Deese [1,2] begins by calculating eigenvalues at the cell centers. The values of the flow variables used in the E

flux calculations at cell face (i+1/2,j) are then determined using the eigenvalues at points (i,j) and (i+1,j). Thus, when

$$(\tilde{\lambda}^{\eta}_{\ell})_{ij} \geq 0 \qquad (\tilde{\lambda}^{\eta}_{\ell})_{ij} < 0 \qquad (25)$$

$$(\tilde{\lambda}^{\eta}_{\ell})_{i+1j} \geq 0 \qquad (\tilde{\lambda}^{\eta}_{\ell})_{i+1j} < 0 \qquad (26)$$

use backward extrapolation — use forward extrapolation

and when

$$\text{sign } (\tilde{\lambda}^{\eta}_{1})_{ij} \neq \text{sign } (\tilde{\lambda}^{\eta}_{1})_{i+1j}$$

average forward/backward exptrapolation (27)

where $\ell = 1,3$. Similar extrapolations are used for the F flux calculations.

The method suggested by Whitfield [3] begins by averaging the flow variables at adjacent cell centers to the cell boundaries. This allows the eigenvalues to be calculated directly at cell boundaries, resulting in less complication than Deese's method. For the E flux calculation at cell face (i+1/2j):

$$(\tilde{\lambda}^{\eta}_{\ell})_{i+1/2j} \geq 0 \quad (28) \qquad (\tilde{\lambda}^{\eta}_{\ell})_{i+1/2j} < 0 \quad (29)$$

use backward extrapolation — use forward extrapolation

Similar extrapolations are used for F flux calculations.

STEGER-WARMING FLUX-VECTOR SPLITTING

In the Steger-Warming Flux-Vector-Splitting method [4], the Euler equations are cast into a slightly different form. First, the eigenvalues are decomposed into non-negative and non-positive components:

$$\tilde{\lambda}_i = \tilde{\lambda}^{+}_i + \tilde{\lambda}^{-}_i \qquad \tilde{\sigma}_1 = \tilde{\sigma}^{+}_i + \tilde{\sigma}^{-}_i \qquad (30)$$

$$\tilde{\lambda}^{\pm}_i = (\tilde{\lambda}_i \pm |\tilde{\lambda}_i|)/2 \qquad \tilde{\sigma}^{\pm}_i = (\tilde{\sigma}_i \pm |\tilde{\sigma}_i|)/2 \qquad (31)$$

Splitting of the eigenvalue allows the E flux vector to be written as:

$$\bar{E} = S_{\xi}\,(\Lambda^{+} + \Lambda^{-})\,S^{-1}_{\xi}\,\bar{Q} = (A^{+} + A^{-})\,\bar{Q} = \bar{E}^{+} + \bar{E}^{-} \qquad (32)$$

where

$$\Lambda = \begin{bmatrix} \tilde{\lambda}_1 & 0 & 0 & 0 \\ 0 & \tilde{\lambda}_2 & 0 & 0 \\ 0 & 0 & \tilde{\lambda}_3 & 0 \\ 0 & 0 & 0 & \tilde{\lambda}_4 \end{bmatrix} \qquad (33)$$

and S_{ξ} and S^{-1}_{ξ} are matrices which diagonalize the A matrix. Similarly for the $\bar{F}$ vector:

$$\bar{F} = \bar{F}^{+} + \bar{F}^{-} \qquad (34)$$

The flux vectors can then be expressed in terms of the eigenvalues of their Jacobian matrices. Thus, in the transformed domain:

$$\bar{E}_1 = \frac{\rho}{2\gamma}\,(2(\gamma - 1)\,\tilde{\lambda}_1 + \tilde{\lambda}_3 + \tilde{\lambda}_4) \qquad (35)$$

$$\bar{E}_2 = \frac{\rho}{2\gamma}\,\{2(\gamma - 1)\tilde{\lambda}_1(y_{\eta}U + x_{\eta}V) + \tilde{\lambda}_3(x_{\eta}V + y_{\eta}(U + a_{\xi})) + \tilde{\lambda}_4(x_{\eta}V + y_{\eta}(U - a_{\xi}))\} \qquad (36)$$

$$\bar{E}_3 = \frac{\rho}{2\gamma}\,\{2(\gamma - 1)\tilde{\lambda}_1(y_{\eta}V - x_{\eta}U) + \tilde{\lambda}_3(y_{\eta}V - x_{\eta}(U + a_{\xi})) + \tilde{\lambda}_4(y_{\eta}V - x_{\eta}(U - a_{\xi}))\} \qquad (37)$$

$$\bar{E}_4 = \frac{\rho}{2\gamma}\,\{(\gamma - 1)\tilde{\lambda}_1(U^2 + V^2) + R + \frac{\tilde{\lambda}_3}{2}\,((U + a_{\xi})^2 + V^2) + \frac{\tilde{\lambda}_4}{2}((U - a_{\xi})^2 + V^2)\} \qquad (38)$$

where

$$R = \frac{(3 - \gamma)(\tilde{\lambda}_3 + \tilde{\lambda}_4)a^2_{\xi}}{2(\gamma - 1)} \qquad (39)$$

and

$U = (uy_{\eta} - vx_{\eta})/s_{\eta}$ = velocity normal to constant ξ lines

$V = (vx_{\eta} - uy_{\eta})/s_{\eta}$ = velocity tangent to constant ξ lines

The forward and backward fluxes are then formed by substituting:

$$\tilde{\lambda}_i = \tilde{\lambda}^{+}_i,\ \tilde{\lambda}^{-}_i \qquad (40)$$

into Eq. 35-39. Again, similar equations are defined for the F flux. The flow variables are extrapolated from cell centers to cell boundaries for the flux calculations. This is known as the MUSCL (Monotone Upstream-Centered Scheme for Conservation Laws) approach. An alternate approach is to calculate the fluxes at the cell centers, then extrapolate the flux values to the cell boundaries. This second approach has been shown to create oscillations in flow solutions [4]. Therefore, the second approach is not considered in this study. One drawback to Steger-Warming Flux-Vector-Splitting method is that the fluxes are not continuously differentiable when eigenvalues change sign, as is the case at sonic points [4].

VAN LEER ET AL FLUX-VECTOR-SPLITTING

In an effort to split the fluxes so that the forward and backward fluxes transition smoothly when eigenvalues change sign, Van Leer et al [5] developed another form of split fluxes. As with Steger's form, Van Leer's splitting method decomposes eigenvalues into non-negative and non-positive parts. The formulas for the E flux are:

$$\bar{E}_1^{\pm} = \pm \frac{\rho}{4a_\xi} (U \pm a_\xi)^2 \tag{41}$$

$$\bar{E}_2^{\pm} = \pm \frac{\rho}{4a_\xi} (U \pm a_\xi)^2 \{x_n V + y_n [((\gamma - 1)U \pm 2a_\xi)/\gamma]\} \tag{42}$$

$$\bar{E}_3^{\pm} = \pm \frac{\rho}{4a_\xi} (U \pm a_\xi)^2 \{y_n V - x_n [((\gamma-1)U \pm 2a_\xi)/\gamma]\}$$

$$\bar{E}_4^{\pm} = \pm \frac{\rho}{4a_\xi} (U \pm a_\xi)^2 \{[(\gamma - 1)U \pm 2a_\xi]^2 / [2(\gamma^2 - 1)] + \frac{V^2}{2}\} \tag{43}$$

where U and V are defined as for Eq. 35-38 and

$$\bar{E}^+ = \bar{E}, \quad \bar{E}^- = 0 \text{ for } M_x \geq 1$$

$$\bar{E}^+ = 0, \quad \bar{E}^- = \bar{E} \text{ for } M_x \leq -1$$

The splitting for F is obtained similarly. As before, the flow variables are extrapolated from cell centers to cell boundaries where the fluxes are calculated (MUSCL approach).

NUMERICAL DISSIPATION AND FLUX-VECTOR-SPLITTING

While upwind (flux-vector-splitting) schemes require no explicitly added dissipation, it would be misleading to state that they do not generate numerical dissipation. For example, consider a scalar equation solved with first order backward differences:

$$\frac{u_i - u_{i-1}}{\Delta x} = \left(\frac{\partial u}{\partial x}\right)_{FO} + O(\Delta x) \tag{44}$$

where FO refers to a first order accurate difference. Equation (44) can be expanded in Taylor series as follows:

$$\frac{u_i - u_{i-1}}{\Delta x} = \frac{u_{i+1} - u_{i-1}}{2\Delta x} - \frac{\Delta x}{2} \frac{u_{i+1} - 2u_i + u_{i-1}}{(\Delta x)^2} \tag{45}$$

The last two terms of the right hand side of Eq. 45 can be viewed as second order accurate differences for the first and second derivatives. Thus, one can consider the first order difference operator in Eq. 44 as the second order representation:

$$\frac{u_i - u_{i-1}}{\Delta x} = \left(\frac{\partial u}{\partial x}\right)_{SO} - \frac{\Delta x}{2} \left(\frac{\partial^2 u}{\partial x^2}\right)_{SO} + O(\Delta x)^2 \tag{46}$$

where SO refers to a second order accurate expression. This shows the first order backward difference operator in Eq. 44 to be equivalent to a second order accurate central difference plus a second order viscous-like term in which the numerical viscosity is proportional to the grid spacing. A similar type of analysis has been used to show that second order upwind differences used to solve Eqns. (2) can be rewritten as a second order central difference plus a fourth-difference viscous-like term [7].

CENTRAL DIFFERENCE SCHEMES

The conservative form of the Euler equations (Eqs. 2 and 13) can also be solved using central difference methods, such as Jameson's finite volume version [6] of the rational Runge-Kutta time-stepping scheme [8]. In central difference schemes, flow variables are calculated at cell boundaries by averaging values from adjacent cell centers.

ARTIFICIAL DISSIPATION MODEL (AD)

For central difference schemes requiring explicitly added dissipation, the calculation of all the artificial dissipation terms is performed according to [6]:

$$dQ = d_\xi Q + d_n Q \tag{47}$$

where d is the dissipation operator and Q is the vector defined in Eq. 2. The two terms on the right hand side of Eq. 47 are contributions from the two computational directions. They can be written as:

$$d_\xi Q = d_{i+1/2j} - d_{i-1/2j} \; ; \; d_n Q = d_{ij+1/2} - d_{ij-1/2} \tag{48}$$

The terms on the right hand sides of Eq. 48 are similar [6]:

$$d_{i+1/2j} = \frac{D_{i+1/2j}}{\Delta t} \{\varepsilon^{(2)}_{i+1/2j} (Q_{i+1j} - Q_{ij}) - \varepsilon^{(4)}_{i+1/2j} (Q_{i+2j} - 3Q_{i+1j} + 3Q_{ij} - Q_{i-1j})\} \tag{49}$$

where the second and fourth order coefficients multiplying the flux derivative terms are flow adaptive coefficients. The scaling with the area D and local time step, Δt, are included to correspond to the formulation of the Euler equations in the transformed plane. A pressure sensor is introduced to locate regions requiring large amounts of artificial viscosity [6]:

$$\nu_{ij} = \frac{|p_{i+1j} - 2p_{ij} + p_{i-1j}|}{p_{i+1j} + 2p_{ij} + p_{i-1j}} \tag{50}$$

The flow adaptive coefficients are then calculated [6] as:

$$\varepsilon^{(2)}_{i+1/2j} = k^{(2)} \max(\nu_{i+1j}, \nu_{ij})$$

$$\varepsilon^{(4)}_{i+1/2j} = \max(0, (k^{(4)} - \varepsilon^{(2)}_{i+1/2j}))$$

$$\text{where } k^{(2)} = 1/4 \text{ and } k^{(4)} = 1/256 \tag{51}$$

PHYSICALLY BASED DISSIPATION (PBD) MODEL

Instead of using an intuitive non-physical formulation for explicitly added dissipation terms, it is suggested that the dissipation be based on actual physical dissipation [9,10,11]. Thus, in order to solve the Euler equations one should actually solve the complete Navier-Stokes equations of viscous and heat conducting flow subject to perfect slip boundary conditions and utilizing spatially varying coefficients of viscosity. The PBD model represents a physically consistent formulation since the Euler equations represent a limiting case of the Navier-Stokes equations as the Reynolds number approaches infinity.

The Navier-Stokes equations of viscous, laminar motion allowing for heat conduction (assuming Fourier's law), expressed in non-dimensional form and transformed coordinates can be summarized as:

$$\frac{\partial \bar{Q}}{\partial t} + \frac{\partial \bar{E}}{\partial \xi} + \frac{\partial \bar{F}}{\partial \eta} = \frac{1}{R_e}\left(\frac{\partial E^v}{\partial \xi} + \frac{\partial F^v}{\partial \eta}\right) \tag{52}$$

where R_e is the Reynolds number and the right hand side fluxes incorporate physically dissipative terms due to shear viscosity, μ, secondary viscosity, λ, and heat conductivity, k. The generalized viscous flux vectors are given by:

$$E^v = [0,\ (y_\eta \tau_{xx} - x_\eta \tau_{xy})/D,(y_\eta \tau_{xy} - x_\eta \tau_{yy})/D,(y_\eta \beta_x - x_\eta \beta_y)/D]^* \tag{53}$$

$$F^v = [0,\ (x_\xi \tau_{xy} - y_\xi \tau_{xx})/D,(x_\xi \tau_{yy} - y_\xi \tau_{xy})/D,(x_\xi \beta_y - y_\xi \beta_x)/D]^* \tag{54}$$

where the shear stress terms:

$$\tau_{xx} = \bar{\mu} u_x + \lambda v_y = [\bar{\mu}(u_\xi y_\eta - u_\eta y_\xi) + \lambda(v_\eta x_\xi - v_\xi x_\eta)]/D \tag{55}$$

$$\tau_{yy} = \bar{\mu} v_y + \lambda u_x = [\bar{\mu}(v_\eta x_\xi - v_\xi x_\eta) + \lambda(u_\xi y_\eta - u_\eta y_\xi)]/D \tag{56}$$

$$\tau_{xy} = \mu(u_y + v_x) = [\mu(v_\xi y_\eta - v_\eta y_\xi + u_\eta x_\xi - u_\xi x_\eta)]/D \tag{57}$$

and the energy equation parameters are

$$\beta_x = u\tau_{xx} + v\tau_{xy} + \frac{\mu}{(\gamma - 1)M_\infty^2 P_r}(T_\xi y_\eta - T_\eta y_\xi)/D \tag{58}$$

$$\beta_y = u\tau_{xy} + v\tau_{yy} + \frac{\mu}{(\gamma - 1)M_\infty^2 P_r}(T_\eta x_\xi - T_\xi x_\eta)/D \tag{59}$$

Here, M_∞ is the free-stream Mach number, P_r is the Prandtl number and T is the absolute temperature. In addition, the longitudinal viscosity coefficient is defined as:

$$\bar{\mu} = 2\mu + \lambda \tag{60}$$

Rankine-Hugoniot shock jump conditions (adiabatic shocks) are guaranteed only [10] if Stokes hypothesis:

$$\lambda = -\frac{2}{3}\mu \tag{61}$$

is enforced for diatomic gases. This relation was used in actual computations.

In devising a PBD model, the coefficient of viscosity must be allowed to vary throughout the flowfield. The existing dissipation sensor is based on the second derivative [6] of the pressure (Eq. 50).

We have decided to use the dissipation sensor that is based on the first derivative of pressure. Thus,

$$\nu_{i+1/2j} = \left|\frac{\partial p}{\partial \xi}\right| = |p_\xi| = |p_{i+1j} - p_{ij}| \tag{62}$$

Through numerical experimentation it has been determined that a more robust sensor is obtained if Eq. 62 is scaled by the local area and the time step as was done in Eq. 49. A modified form of first derivative of pressure sensor can be calculated as the average of the first derivative of the pressure at three or five neighboring cell faces. For example, instead of using equation (62), one can use

$$\nu_{i+1/2j} = |p_{\xi i-3/2j} + p_{\xi i-1/2j} + p_{\xi i-1/2j} + p_{\xi i+3/2j} + p_{\xi i+5/2j}|/5 \tag{63}$$

By using the average over five neighboring cell faces, unwanted "spikes" in the magnitude of the viscosity coefficient can be avoided. Other viscosity sensors are discussed in reference [11]. We used R_e between 2 and 10.

The main differences between the PBD model [8] and the existing artificial dissipation model [6] can be summarized as follows:

1) The artificial dissipation model [6] introduces a non-physical source term into the continuity equation, while the PBD model leaves the continuity equation intact.
2) The PBD model does not require fourth order dissipation.
3) The second order dissipation used in the PBD model is constructed from the actual physical dissipation which is always non-negative.
4) A computer code incorporating the PBD model into the Euler equations can be easily converted to a Navier-Stokes solver by enforcing no-slip boundary conditions and by using physical values for the viscosity coefficients.

INTEGRATION SCHEMES

The integration scheme used with the Flux-Vector-Splitting methods is based on a modified second order MacCormack [13] scheme in which both the predictor and corrector steps use upwind differences. The scheme is second order accurate in both time and space. A linear stability analysis of the scheme shows it to be stable for a CFL number less than or equal to 2. The time integration algorithm used with the central difference schemes utilizing artificial and physical dissipation models, is a four-step rational Runge-Kutta method [8]. A linear stability analysis shows the system to be stable for a CFL number less than or equal to 2.8. Having established the stability limit of a scheme, the maximum time step for each iteration can be determined. Referring again to the two-dimensional Euler equations in the transformed plane:

$$\Delta t = \frac{t_\xi t_\eta}{t_\xi + t_\eta} \tag{64}$$

where

$$t_\xi = \frac{CFL\Delta\xi}{\max_i(\tilde{\lambda}_i)} \qquad t_\eta = \frac{CFL\Delta\eta}{\max_i(\tilde{\sigma}_i)}$$

The time step for each cell is determined from the local linear stability conditions. The use of local time steps implies that the procedure will not be time accurate, but the convergence rate will be improved.

BOUNDARY CONDITIONS

The farfield boundary conditions are calculated using Riemann invariants (assumed to be locally one-dimensional), which can be derived with the aid of the one-dimensional equations of motion written in the form [13]:

$$\frac{2}{\gamma-1}\left(\frac{\partial a}{\partial t} + u\frac{\partial a}{\partial x}\right) + a\frac{\partial u}{\partial x} = 0 \;;\; \frac{\partial u}{\partial t} + u\frac{\partial u}{\partial x} + \frac{2a}{\gamma-1}\frac{\partial a}{\partial x} = 0 \tag{66}$$

Adding and subtracting Eq. 66 yields

$$\left\{\frac{\partial}{\partial t} + (u+a)\frac{\partial}{\partial x}\right\}\left(u + \frac{2a}{\gamma-1}\right) = 0$$

$$\left\{\frac{\partial}{\partial t} + (u-a)\frac{\partial}{\partial x}\right\}\left(u - \frac{2a}{\gamma-1}\right) = 0 \tag{67}$$

From Eq. 67 it can be shown that invariants are

$$R1 = u + \frac{2a}{\gamma-1} \qquad R2 = u - \frac{2a}{\gamma-1} \tag{68}$$

Equations (68) are constant on the curves with the slopes:

$$\frac{dx}{dt} = u + a \qquad \frac{dx}{dt} = u - a \tag{69}$$

By adding Eqs. 68, the normal velocity at the boundary can be calculated. Subtracting Eqs. 68 yields the speed of sound. Then, depending on the direction of the normal velocity, the entropy and tangential velocity are defined from the upwind side by either using free-stream values or extrapolating from the interior of the computational domain.

The solid wall boundary condition implies that the normal velocity at the solid boundary is zero:

$$(q_n)_{boundary} = 0 \tag{70}$$

Accordingly, for the normal direction (in Cartesian form):

$$\sigma_1 = \sigma_2 = q_n = 0 \qquad \sigma_3 = q_n + a = a$$

$$\sigma_4 = q_n - a = -a \tag{71}$$

Equations (71) suggest that only one flow quantity is needed on the surface; the pressure is extrapolated using the normal momentum equation. The normal momentum can be obtained from the x and y momentum equations:

$$\text{x-mom.} \qquad n_x\left(\frac{\partial u}{\partial t} + u\frac{\partial u}{\partial x} + v\frac{\partial u}{\partial y} + \frac{1}{\rho}\frac{\partial p}{\partial x}\right) = 0 \tag{72}$$

$$\text{y-mom.} \qquad n_y\left(\frac{\partial v}{\partial t} + u\frac{\partial v}{\partial x} + v\frac{\partial v}{\partial y} + \frac{1}{\rho}\frac{\partial p}{\partial y}\right) = 0 \tag{73}$$

Upon adding Eqs. 72 and 73, the normal momentum equation is:

$$n_x\frac{\partial u}{\partial t} + n_y\frac{\partial v}{\partial t} + u\left(n_x\frac{\partial u}{\partial x} + n_y\frac{\partial v}{\partial x}\right) +$$

$$v\left(n_x\frac{\partial u}{\partial y} + n_y\frac{\partial u}{\partial y}\right) + \frac{1}{\rho}\frac{\partial p}{\partial n} = 0 \tag{74}$$

$$\frac{1}{\rho}\frac{\partial p}{\partial n} = \frac{1}{\rho}\left(n_x\frac{\partial p}{\partial x} + n_y\frac{\partial p}{\partial y}\right)$$

$$\hat{n} = (n_x, n_y) = \text{direction cosines} \tag{75}$$

Then, using Eq. 71 and the chain rule, four auxiliary equations are developed:

$$q_n = \vec{q}\cdot\hat{n} = un_x + vn_y = 0 \qquad \frac{\partial}{\partial t}(un_x + vn_y) = 0 \tag{76}$$

$$\frac{\partial}{\partial x}(un_x + vn_y) = 0 = n_x\frac{\partial u}{\partial x} + n_y\frac{\partial v}{\partial x} + u\frac{\partial n_x}{\partial x} + v\frac{\partial n_y}{\partial x} \tag{77}$$

$$\frac{\partial}{\partial y}(un_x + vn_y) = 0 = n_x\frac{\partial u}{\partial y} + n_y\frac{\partial v}{\partial y} + u\frac{\partial n_x}{\partial y} + v\frac{\partial n_y}{\partial y} \tag{78}$$

Substituting Eqs. 76-78 into Eq. 74 and simplifying yields:

$$\frac{\partial p}{\partial n} = \rho u_i u_j \frac{\partial n}{\partial x_j} \qquad i = 1,2 \qquad j = 1,2 \tag{79}$$

Thus, the pressure at the boundary becomes:

$$p_{BODY} = p_{i,j+1/2} - \frac{\partial p}{\partial n}\Delta n \tag{80}$$

where Δn is the normal distance from the solid boundary. Certain formulations require ghost or imaginary cells located inside the solid boundary. To obtain flow quantities inside these cells, three conditions are specified and one condition is extrapolated. The specified quantities are:

$$(q_n)_{GHOST} = -(q_n)_{ij+1/2}$$

$$(q_t)_{GHOST} = (q_t)_{ij+1/2} \;;\; (h_o)_{GHOST} = (h_{o\infty})_{ij+1/2} \tag{81}$$

while the linearly extrapolated quantity is:

$$p_{GHOST} = 2p_{BODY} - p_{ij+1/2} \tag{82}$$

Once the pressure is known, the density is determined from:

$$\rho = p/\left\{\left(h_{o\infty} - (u^2+v^2)\right)\frac{\gamma-1}{2\gamma}\right\} \tag{83}$$

RESULTS

The first test case chosen to evaluate the Flux-Vector-Splitting (FVS) and central difference schemes involved flow around a NACA 0012 airfoil.

Calculations were performed on a 128x32 C-type grid (Fig. 1). Computations were performed on the NCSA CRAY X/MP-48 at the University of Illinois and run for 2000 iterations. A non-lifting case was tested for a freestream Mach number of $M_\infty = .8$ and an angle of attack of $\alpha = 0°$. To start the computations, the entire domain was set to free-stream conditions and the solid wall boundary conditions were applied impulsively. For comparison purposes the pressure coefficients from the various schemes were plotted against the pressure coefficients obtained with Jameson's scheme. Figs. 2-6 show plots of the surface pressure coefficient for the four FVS schemes and the central difference scheme with the Artificial Dissipation (AD) and Physically Based Dissipation (PBD) models. It is apparent that Van Leer's scheme gives the sharpest shock while Whitfield's scheme yields the most smeared shock. The shocks obtained with the schemes of Steger-Warming and Deese are better than Whitfield's, but not as sharp as Van Leer's. Also note that Whitfield's scheme yields an unusually large post-shock pressure recovery region. The use of PBD model yielded a somewhat sharper shock than the AD model. Note, however, a small overshoot upstream of the shock using the PBD model. Figures 7-12 illustrate the flowfield pressure contours for the FVS and central difference schemes. Again, one can note the unusually large pressure recovery region obtained with Whitfield's scheme. The results obtained with the two dissipation models are very similar. Figures 13-18 present total pressure loss contours for all the schemes. Since the total pressure loss can be related to the entropy, one would expect the contours to resemble streamlines. The FVS schemes appear to develop non-physical total pressure losses near the leading edge. The FVS schemes, with the exception of Van Leer's, also develop small "islands" of total pressure loss downstream of the shock. The results obtained with the PBD model may appear unusual, but the actual values for the total pressure loss ahead of the shock are smaller than those from most of the other schemes.

A lifting case was run for a freestream Mach number of $M_\infty = .80$ and an angle of attack of $\alpha = 1.25°$. Figures 20-24 illustrate the surface pressure coefficient for all the schemes plotted against the results obtained with Jameson's scheme. Note that Van Leer's scheme yields sharp shocks on both the upper and lower surfaces. Again, Whitfield's scheme smears the shocks. The PBD model yields a slightly sharper shock than the AD model on both the upper and lower surfaces. Figures 25-30 show flowfield pressure contours for all the schemes and Figures 31-36 illustrate the total pressure loss contours for all the schemes. Note that using Whitfield's scheme, a complete "boundary layer" has developed near the airfoil surface.

CONCLUSIONS

A comparative study of algorithms for the solution of the Euler equations has been performed using four Flux-Vector-Splitting (FVS) schemes and a central difference scheme with two different dissipation models. All schemes were tested for the case of steady, inviscid, transonic airfoil flow. Van Leer's FVS scheme is robust and appears to generate little numerical dissipation. The FVS schemes of Deese and Steger yield results similar to Van Leer's, though not quite as robust. Whitfield's FVS scheme generates large amounts of numerical dissipation, which smears shocks and causes excessive pressure recovery. A new, Physically Based Dissipation (PBD) model for central difference schemes has been compared to Jameson's Artificial Dissipation (AD) model. The PBD model generates strictly non-negative dissipation. Also PBD does not alter the continuity equation like the AD model, and it does not require fourth order dissipation terms. The PBD model allows an Euler solver to be readily converted to a Navier-Stokes code and can be applied to three-dimensional cases.

ACKNOWLEDGEMENTS

The authors would like to express their sincere appreciation to Ms. Amy Myers for her excellent typing and to Apple Computer and Sun Microsystems for the equipment used in this work.

REFERENCES

1. Deese, J. E., "Numerical Experiments with the Split-Flux-Vector Form of the Euler Equations," AIAA Paper No. 83-0122, January, 1983.

2. Deese, J. E., "Split-Flux Vector Solutions of the Euler Equations for Three-Dimensional Configurations," AIAA paper no. 85-0434, January, 1985.

3. Whitfield, D., "Three-Dimensional Unsteady Euler Equation Solutions Using Flux Vector Splitting," Workshop at University of Tennessee Space Institute, March, 1984.

4. Steger, J. L. and Warming, R. F., "Flux Vector Splitting of the Inviscid Gasdynamic Equations with Application to Finite Difference Methods," Journal of Computational Physics, Vol. 40, April 1981, pp. 263-293.

5. Anderson, W. K., Thomas, J. L., and Van Leer, B., "A Comparison of Finite Volume Flux Vector Splittings for the Euler Equations," AIAA paper no. 85-0122.

6. Jameson, A., Schmidt, W., and Turkel, E., "Numerical Solutions of the Euler Equations by Finite Volume Methods Using Runge-Kutta Time Stepping Schemes," AIAA paper no. 81-1259, 1981.

7. Pulliam, T. H., "Artificial Dissipation Models for the Euler Equations," AIAA paper no. 85-04388, January 1985.

8. Wambecq, A., "Rational Runge-Kutta Method for Solving Systems of Ordinary Differential Equations," Computing, Vol. 20, 1978, pp. 333-342.

9. Dulikravich, G., Dorney, D., and Lee, S., "Iterative Acceleration and Physically Based Dissipation for Euler Equations of Gas Dynamics," presented at the ASME WAM '88 Symposium on Advances and Applications in Computational Fluid Dynamics, Chicago, IL, Nov. 28-Dec. 2, 1988.

10. Dulikravich, G. S., Dorney, D. J. and Lee, S., "Numerical Versus Physical Dissipation in the Solution of Compressible Navier-Stokes Equations," AIAA paper No., 89-0550, Reno, NV, Jan. 9-12, 1989.

11. Dulikravich, G. S. and Dorney, D. J., "Artificial Dissipation Sensors for Computational Dynamics," AIAA paper No. 89-0643, Reno, NV, Jan. 9-12, 1989.

12. Dulikravich, G. S. and Kennon, S. R., "Theory of Unsteady Irrotational Flows Including Heat Conductivity and Longitudinal Viscosity," AIAA paper no. 88-0709, January, 1988; also to appear in International Journal of Mathematical and Computer Modelling, Vol. 10, No. 8, 1988, pp. 583-592.

13. Warming, R. F. and Beam, R. M., "Upwind Second-Order Difference Schemes and Applications in Aerodynamic Flows," AIAA Journal, Vol. 14, Sept. 1976, pp. 1241-1249.

14. Liepmann, H. W. and Roshko, A., Elements of Gasdynamics, New York, Wiley, 1957.

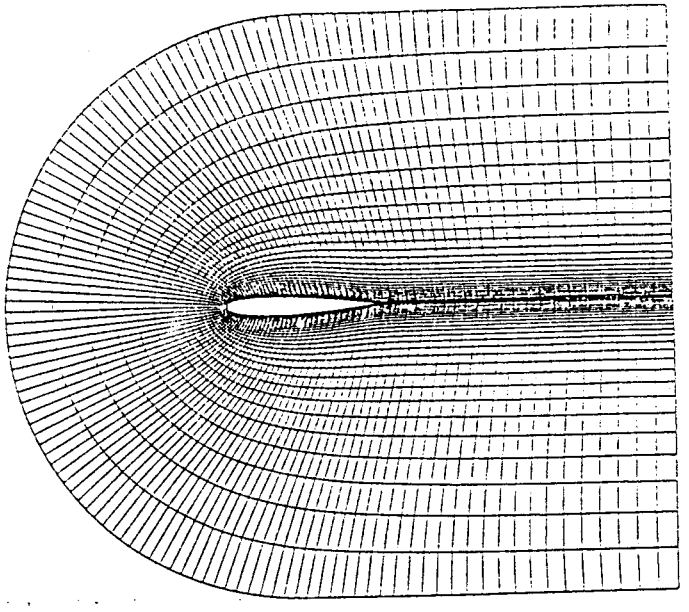

Fig.1 Computational grid: 128 x 32 cells

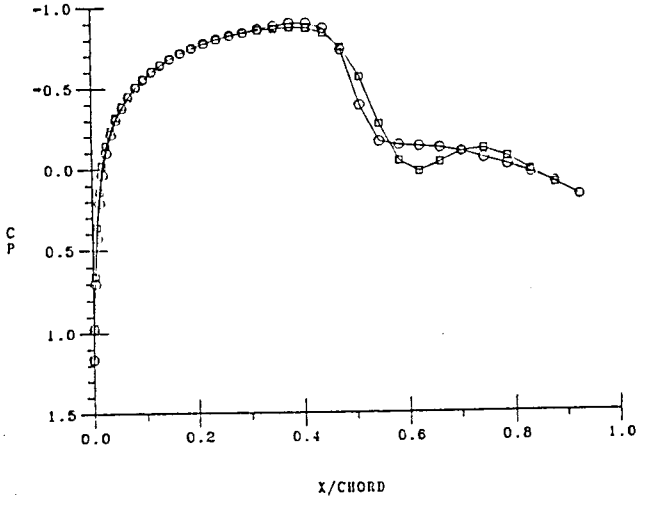

Fig.2 Whitfield's (squares) and Jameson's (circles) surface Cp distribution: NACA 0012; $M_\infty = 0.8$; $\alpha = 0.0°$.

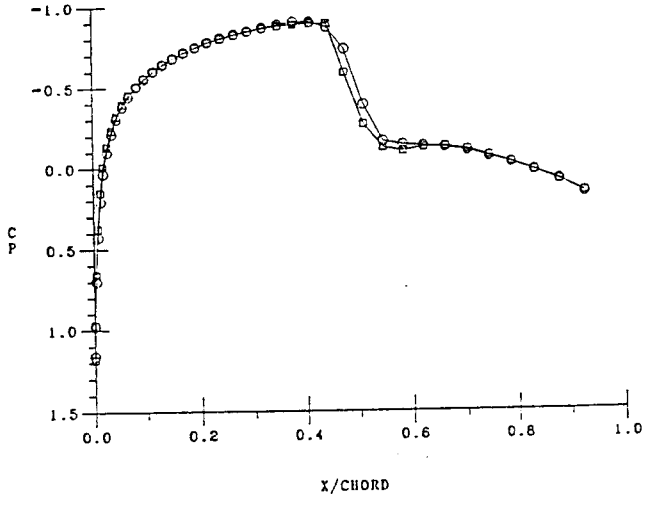

Fig.3 Steger-Warming(squares) and Jameson's (circles) surface Cp distribution: NACA 0012; $M_\infty = 0.8$; $\alpha = 0.0°$.

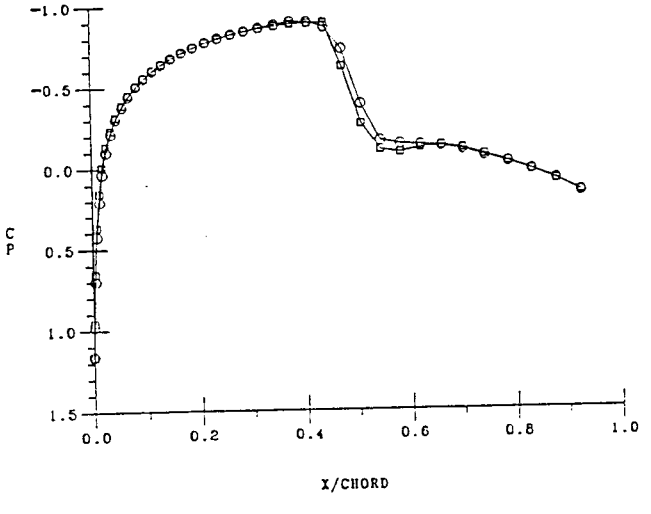

Fig.4 Deese's (squares) and Jameson's (circles) surface Cp distribution: NACA 0012; $M_\infty = 0.8$; $\alpha = 0.0°$.

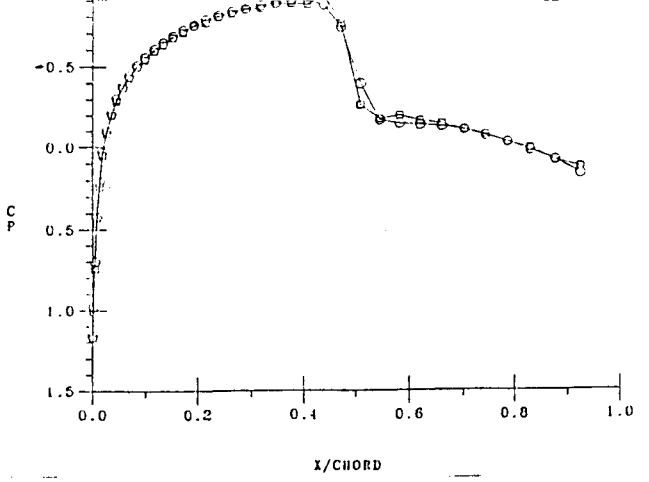

Fig.5 PBD method (squares) and Jameson's (circles) surface Cp distribution: NACA 0012; M_∞= 0.8; α = 0.0°.

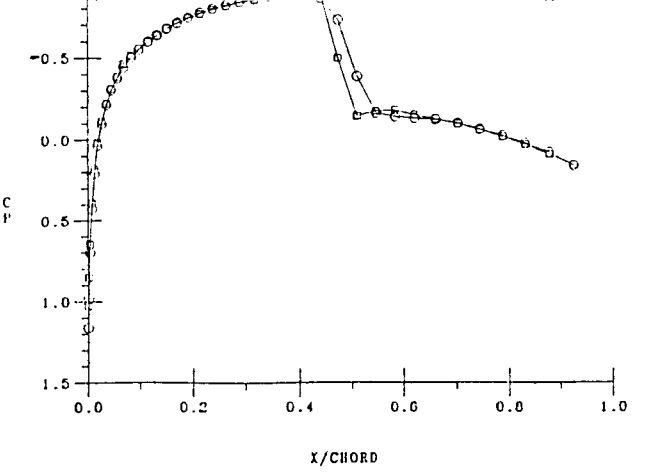

Fig.6 Van Leer's (squares) and Jameson's (circles) surface Cp distribution: NACA 0012; M_∞= 0.8; α = 0.0°.

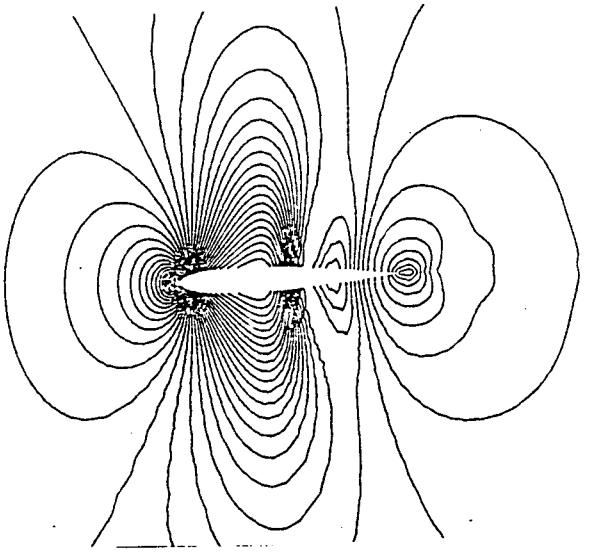

Fig.7 Whitfield's method: isobars for NACA 0012; M_∞= 0.8; α = 0.0°.

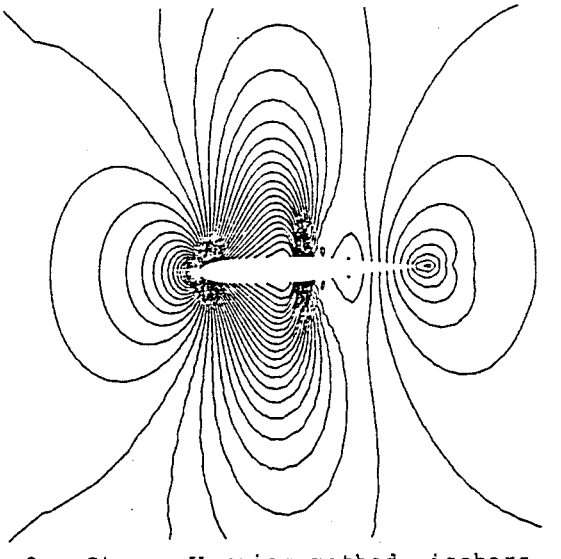

Fig.8 Steger-Warming method: isobars for NACA 0012; M_∞= 0.8; α = 0.0°.

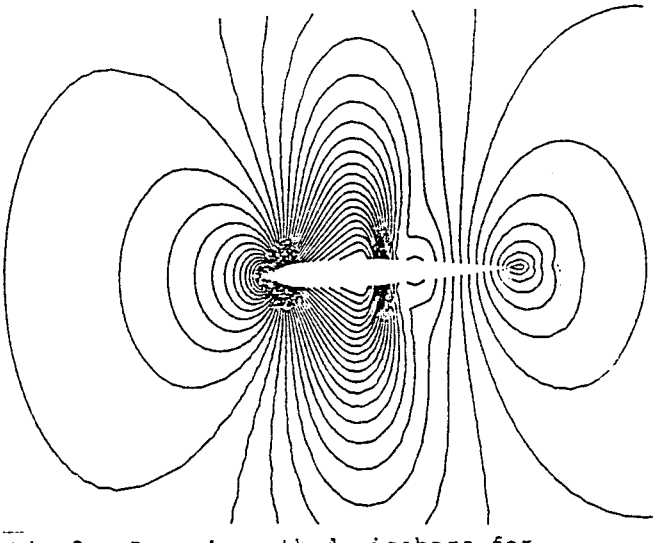

Fig.9 Deese's method: isobars for NACA 0012; M_∞= 0.8; α = 0.0°.

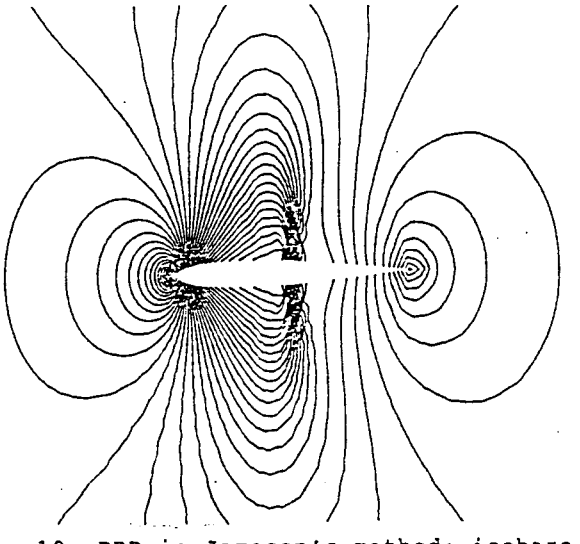

Fig.10 PBD in Jameson's method: isobars for NACA 0012; M_∞= 0.8; α = 0.0°.

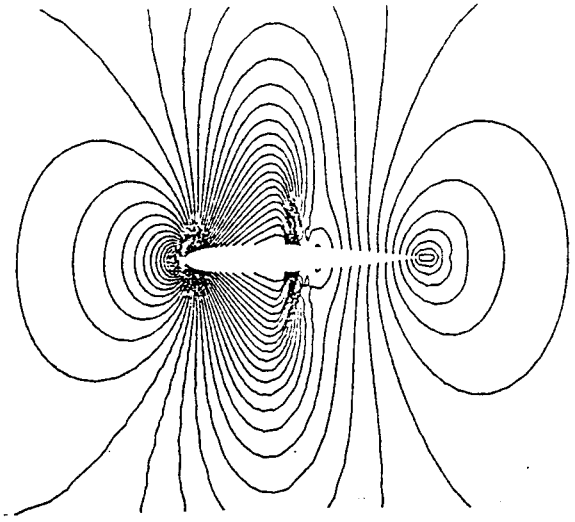

Fig.11 Van Leer's method: isobars for NACA 0012; $M_\infty = 0.8$; $\alpha = 0.0^\circ$.

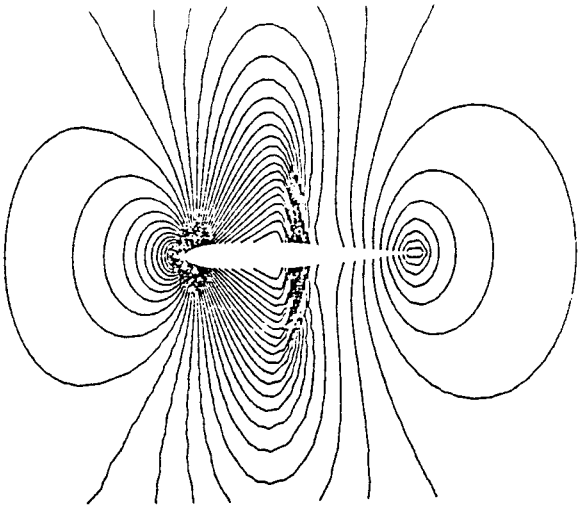

Fig.12 Original Jameson's method: isobars for NACA 0012; $M_\infty = 0.8$; $\alpha = 0.0^\circ$.

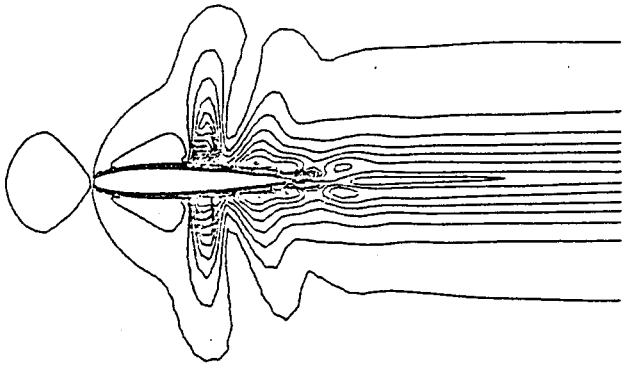

Fig.13 Whitfield's method: total pressure loss for NACA 0012; $M_\infty = 0.8$; $\alpha = 0.0^\circ$.

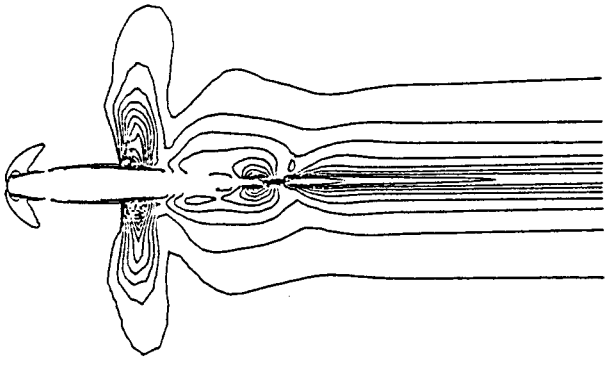

Fig.14 Steger-Warming method: total pressure loss for NACA 0012; $M_\infty = 0.8$; $\alpha = 0.0^\circ$.

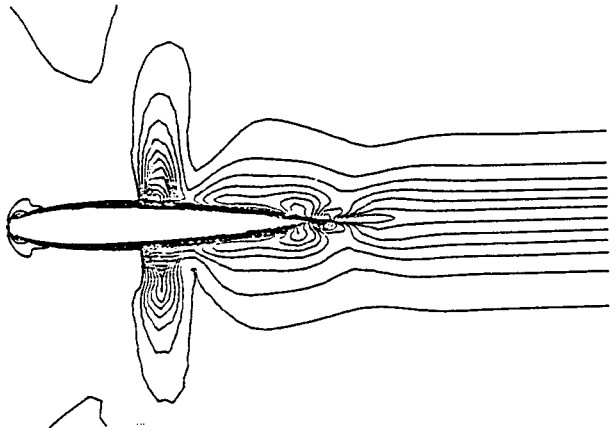

Fig.15 Deese's method: total pressure loss for NACA 0012; $M_\infty = 0.8$; $\alpha = 0.0^\circ$.

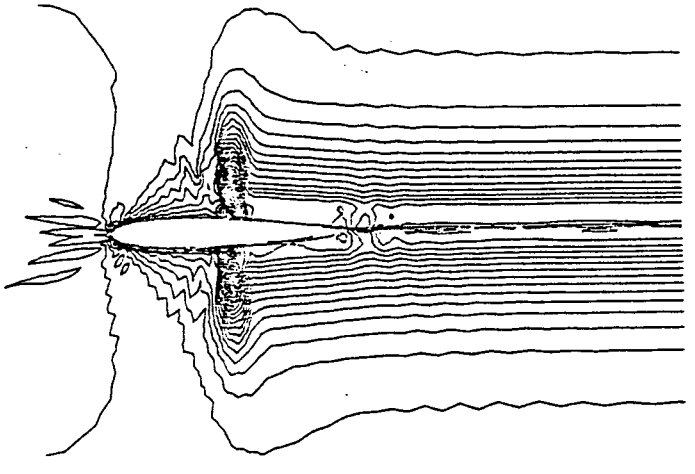

Fig.16 PBD method: total pressure loss for NACA 0012; $M_\infty = 0.8$; $\alpha = 0.0^\circ$.

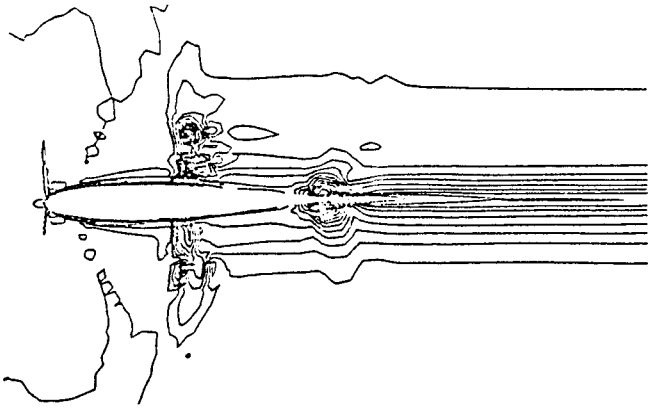

Fig.17 Van Leer's method: total pressure loss for NACA 0012; $M_\infty = 0.8; \alpha = 0.0^\circ$.

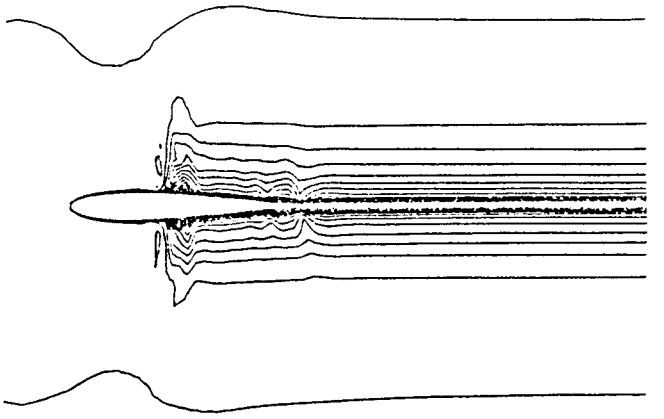

Fig.18 Jameson's method: total pressure loss for NACA 0012; $M_\infty = 0.8; \alpha = 0.0^\circ$.

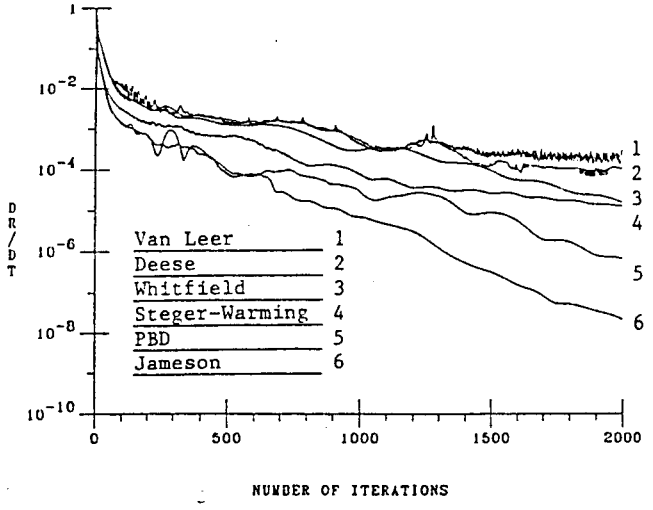

Fig.19 Comparison of convergence histories

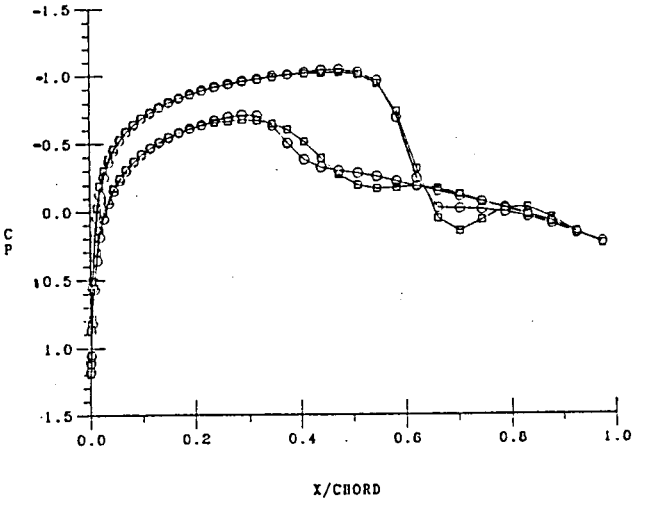

Fig.20 Whitfield's (squares) and Jameson's (circles) surface Cp distribution: NACA 0012; $M_\infty = 0.8; \alpha = 1.25^\circ$.

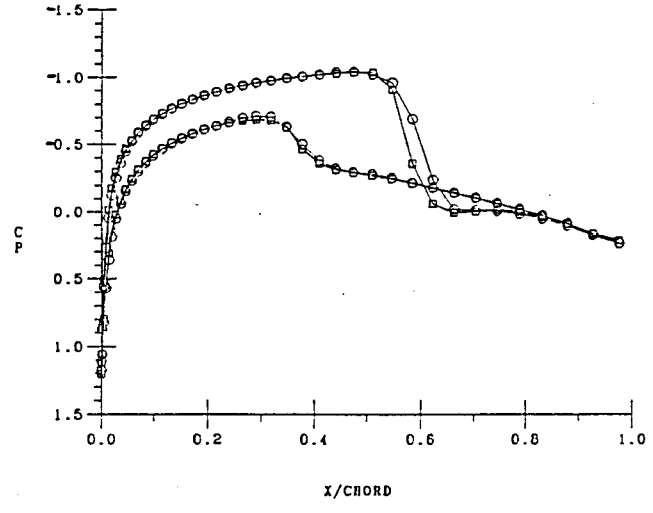

Fig.21 Steger-Warming(squares) and Jameson's (circles) surface Cp distribution: NACA 0012; $M_\infty = 0.8; \alpha = 1.25^\circ$.

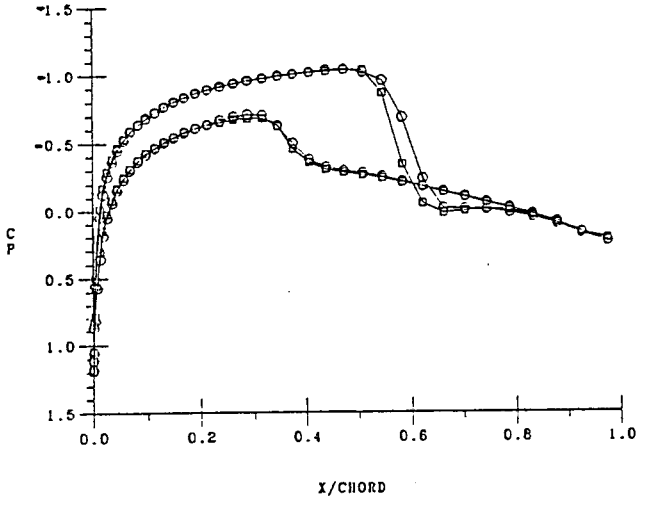

Fig.22 Deese's (squares) and Jameson's (circles) surface Cp distribution: NACA 0012; $M_\infty = 0.8; \alpha = 1.25^\circ$.

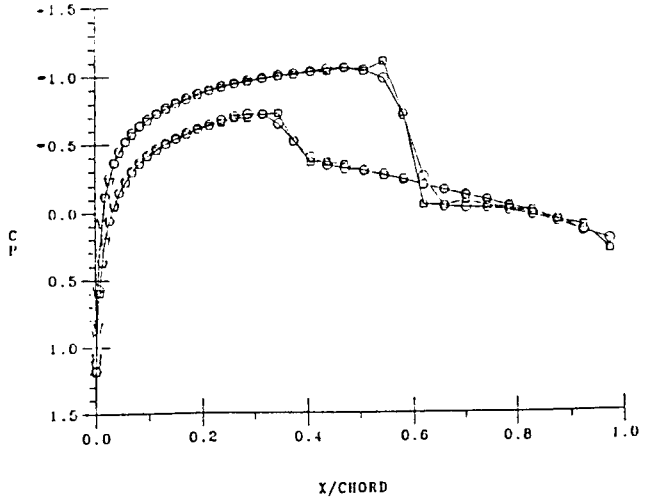

Fig.23 PBD method (squares) and Jameson's (circles) surface Cp distribution: NACA 0012; $M_\infty = 0.8$; $\alpha = 1.25°$.

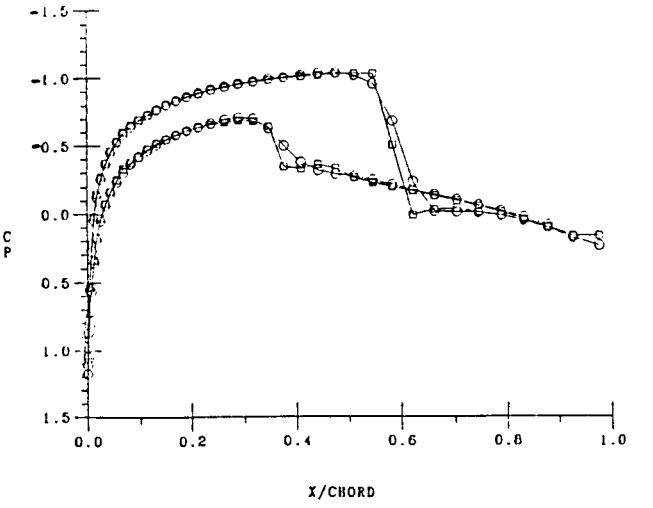

Fig.24 Van Leer's (squares) and Jameson's (circles) surface Cp distribution: NACA 0012; $M_\infty = 0.8$; $\alpha = 1.25°$.

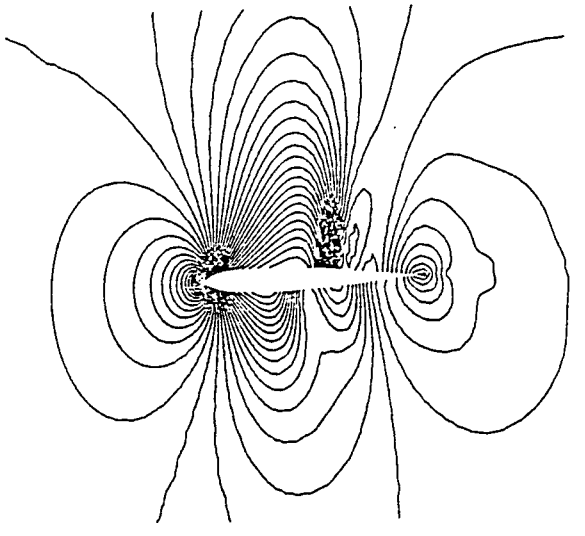

Fig.25 Whitfield's method: isobars for NACA 0012; $M_\infty = 0.8$; $\alpha = 1.25°$.

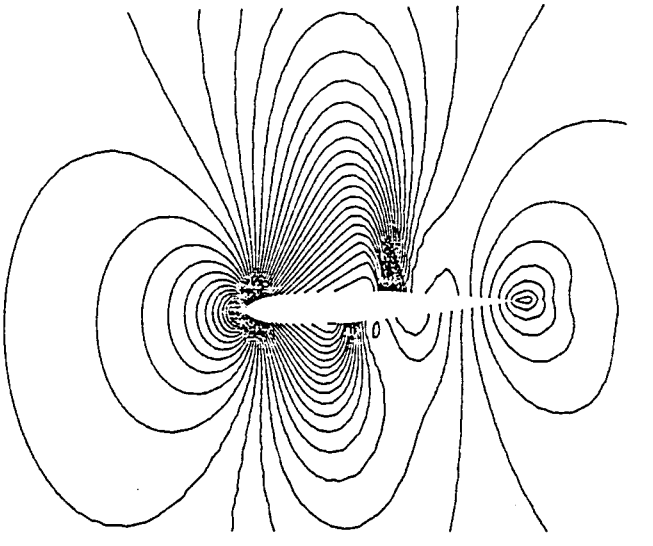

Fig.26 Steger-Warming method: isobars for NACA 0012; $M_\infty = 0.8$; $\alpha = 1.25°$.

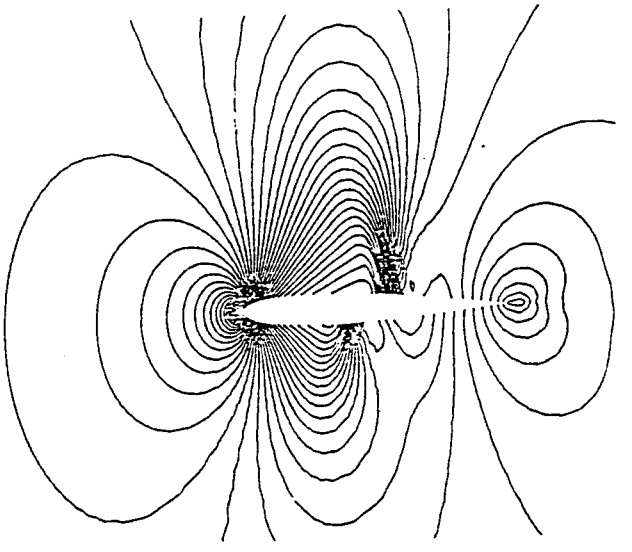

Fig.27 Deese's method: isobars for NACA 0012; $M_\infty = 0.8$; $\alpha = 1.25°$.

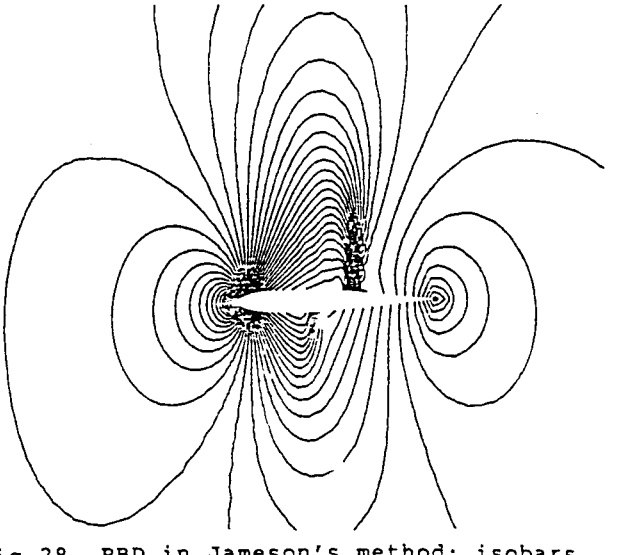

Fig.28 PBD in Jameson's method: isobars for NACA 0012; $M_\infty = 0.8$; $\alpha = 1.25°$.

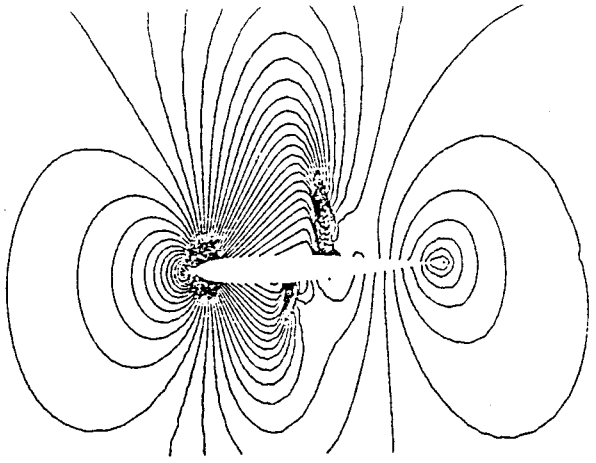

Fig.29 Van Leer's method: isobars for NACA 0012; $M_\infty = 0.8$; $\alpha = 1.25°$.

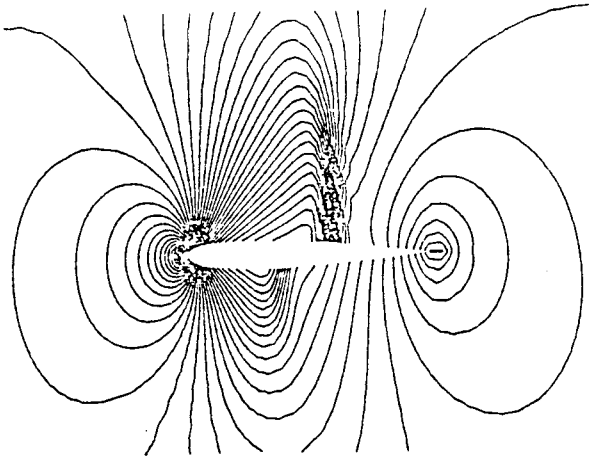

Fig.30 Original Jameson's method: isobars for NACA 0012; $M_\infty = 0.8$; $\alpha = 1.25°$.

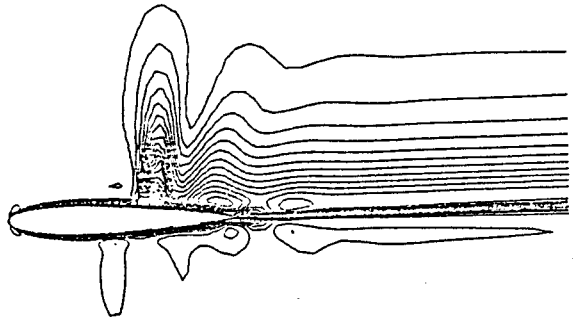

Fig.31 Whitfield's method: total pressure loss for NACA 0012; $M_\infty = 0.8$; $\alpha = 1.25°$.

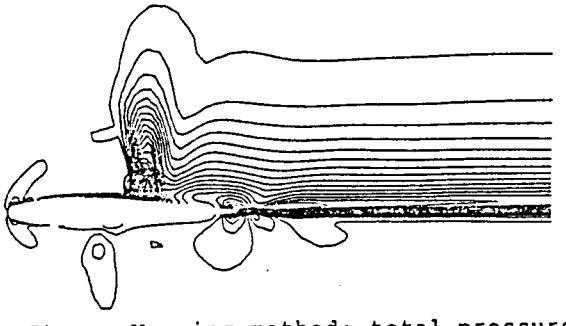

Fig.32 Steger-Warming method: total pressure loss for NACA 0012; $M_\infty = 0.8$; $\alpha = 1.25°$.

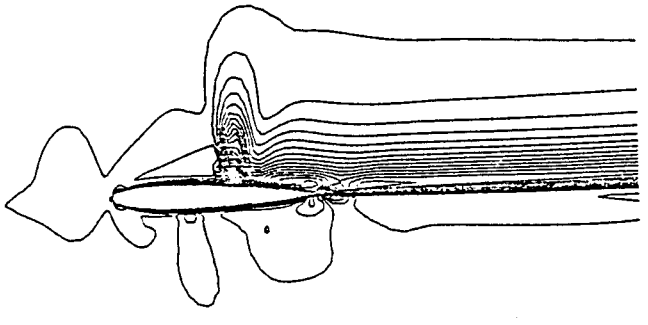

Fig.33 Deese's method: total pressure loss for NACA 0012; $M_\infty = 0.8$; $\alpha = 1.25°$.

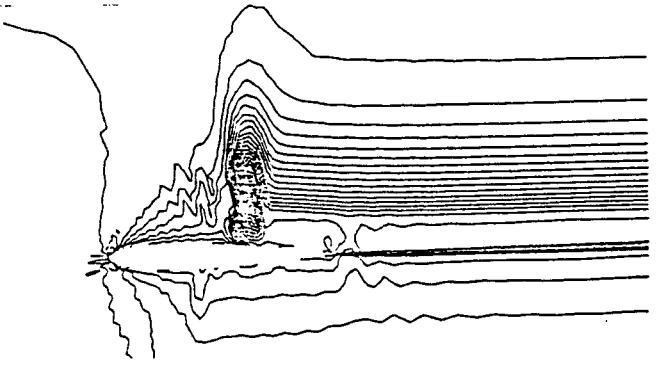

Fig.34 PBD method: total pressure loss for NACA 0012; $M_\infty = 0.8$; $\alpha = 1.25°$.

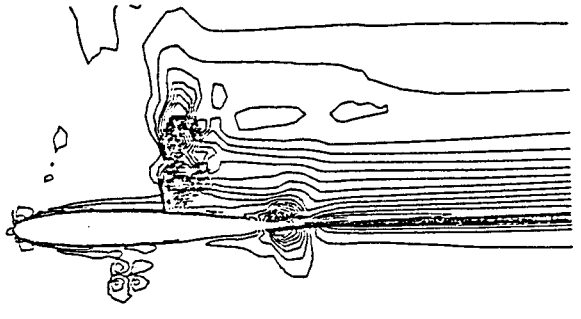

Fig.35 Van Leer's method: total pressure loss for NACA 0012; $M_\infty = 0.8$; $\alpha = 1.25°$.

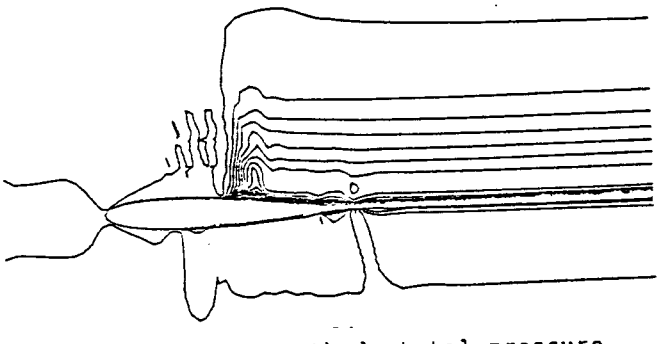

Fig.36 Jameson's method: total pressure loss for NACA 0012; $M_\infty = 0.8$; $\alpha = 1.25°$.

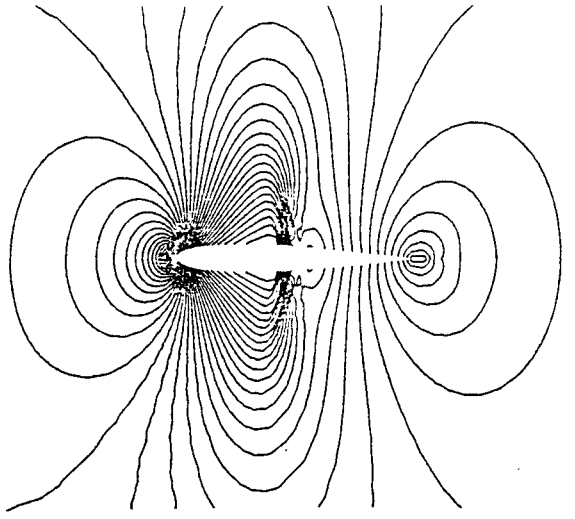

Fig.11 Van Leer's method: isobars for NACA 0012; $M_\infty = 0.8$; $\alpha = 0.0^\circ$.

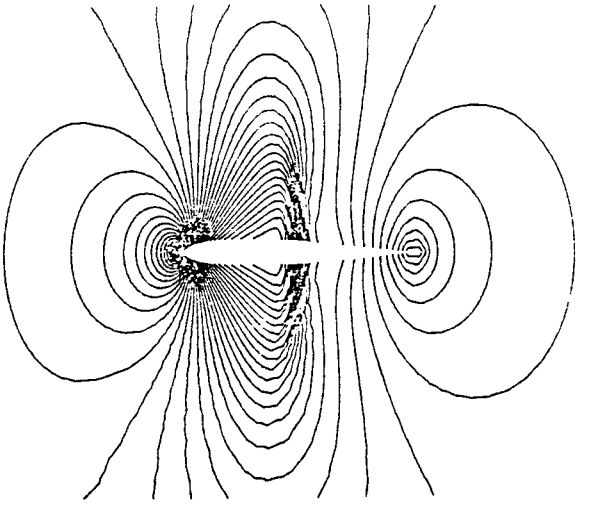

Fig.12 Original Jameson's method: isobars for NACA 0012; $M_\infty = 0.8$; $\alpha = 0.0^\circ$.

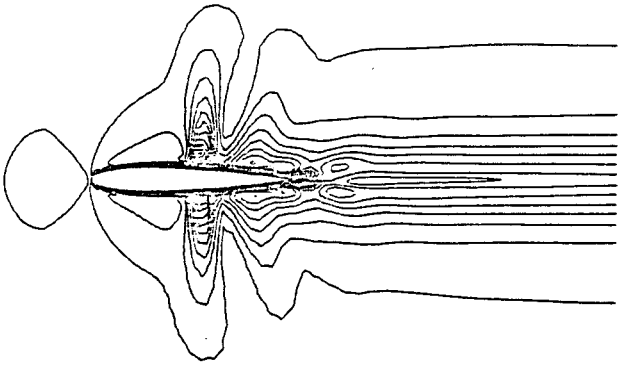

Fig.13 Whitfield's method: total pressure loss for NACA 0012; $M_\infty = 0.8$; $\alpha = 0.0^\circ$.

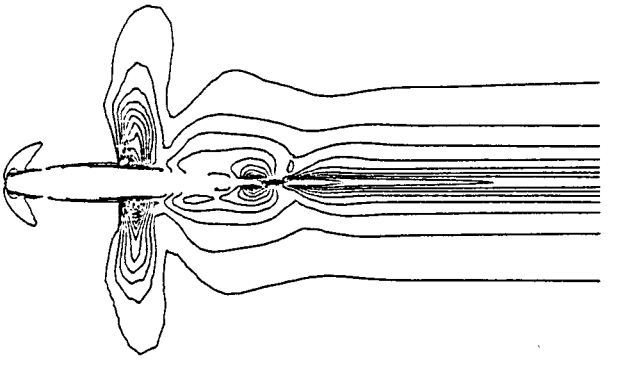

Fig.14 Steger-Warming method: total pressure loss for NACA 0012; $M_\infty = 0.8$; $\alpha = 0.0^\circ$.

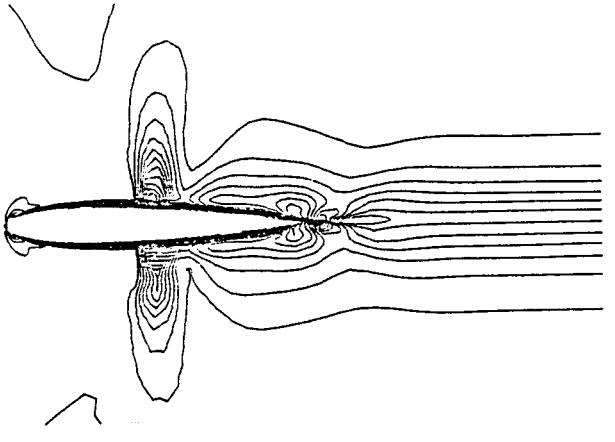

Fig.15 Deese's method: total pressure loss for NACA 0012; $M_\infty = 0.8$; $\alpha = 0.0^\circ$.

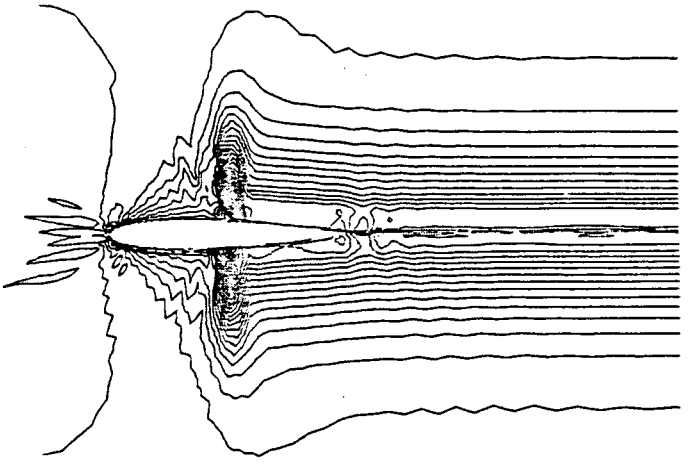

Fig.16 PBD method: total pressure loss for NACA 0012; $M_\infty = 0.8$; $\alpha = 0.0^\circ$.

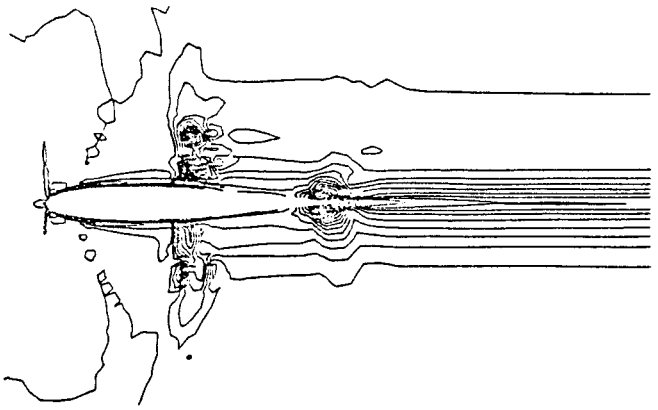

Fig.17 Van Leer's method: total pressure loss for NACA 0012; $M_\infty = 0.8; \alpha = 0.0^\circ$.

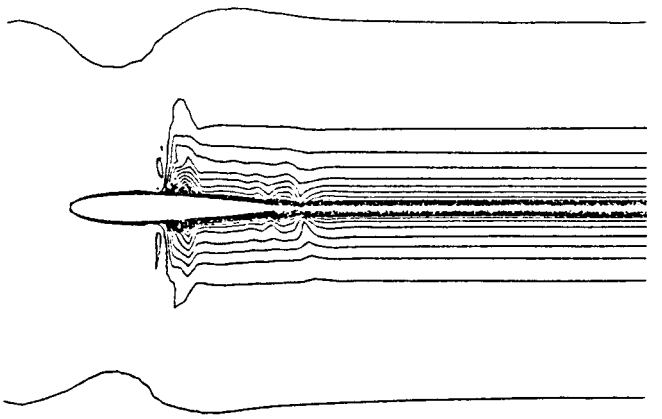

Fig.18 Jameson's method: total pressure loss for NACA 0012; $M_\infty = 0.8; \alpha = 0.0^\circ$.

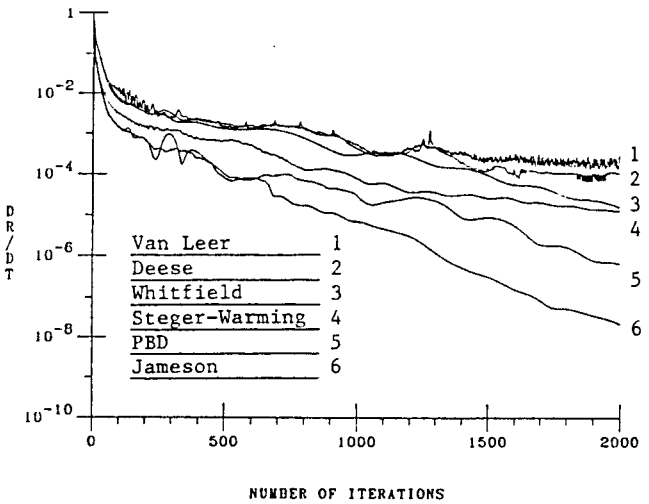

Fig.19 Comparison of convergence histories

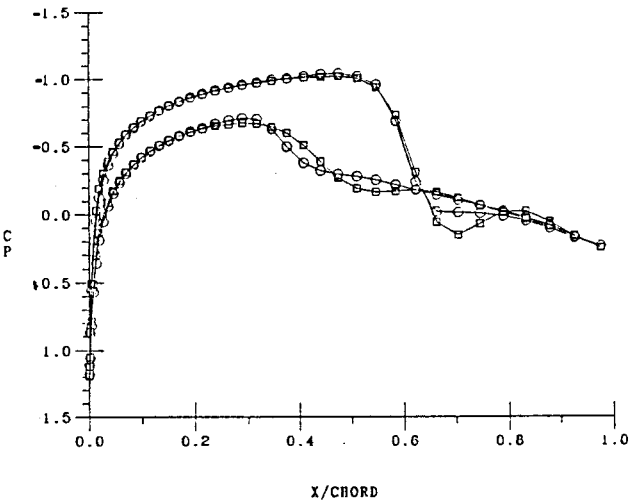

Fig.20 Whitfield's (squares) and Jameson's (circles) surface Cp distribution: NACA 0012; $M_\infty = 0.8$; $\alpha = 1.25^\circ$.

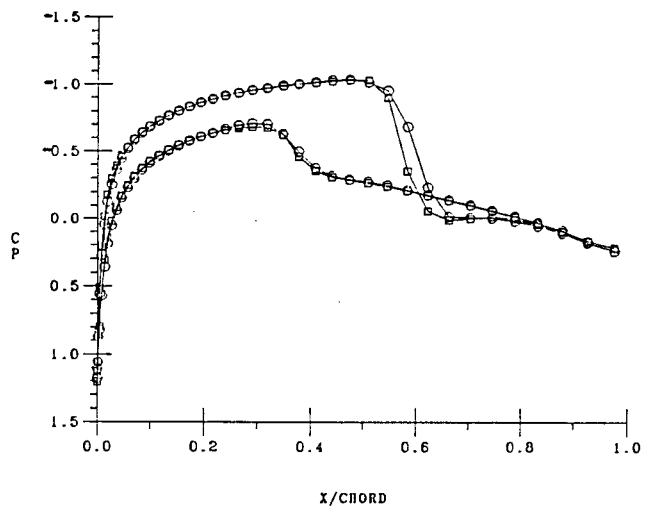

Fig.21 Steger-Warming(squares) and Jameson's (circles) surface Cp distribution: NACA 0012; $M_\infty = 0.8$; $\alpha = 1.25^\circ$.

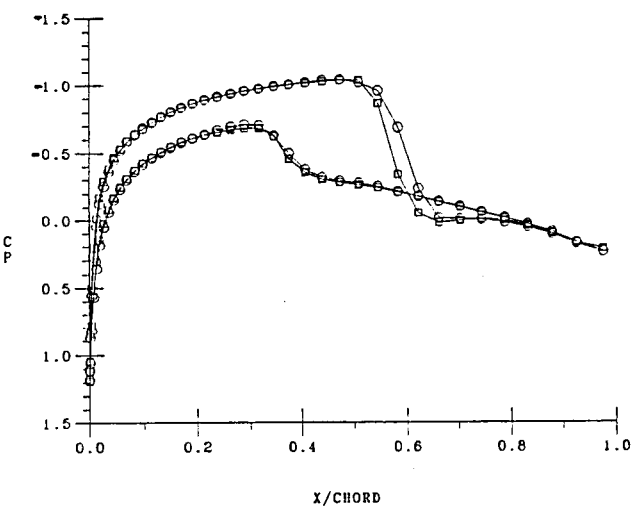

Fig.22 Deese's (squares) and Jameson's (circles) surface Cp distribution: NACA 0012; $M_\infty = 0.8$; $\alpha = 1.25^\circ$.

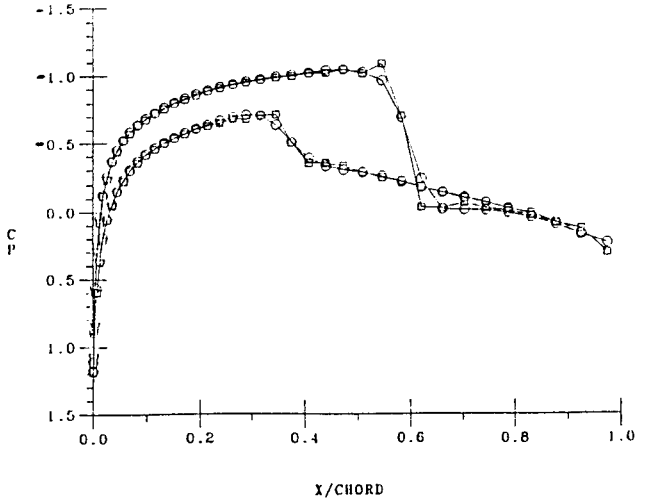

Fig.23 PBD method (squares) and Jameson's (circles) surface Cp distribution: NACA 0012; M_∞= 0.8; α = 1.25°.

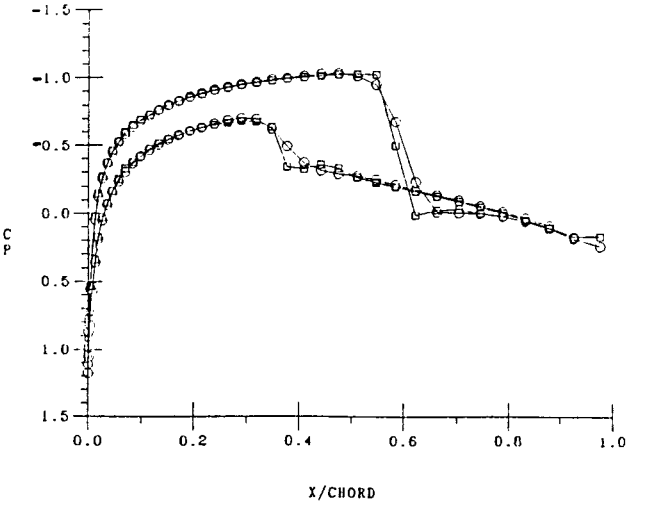

Fig.24 Van Leer's (squares) and Jameson's (circles) surface Cp distribution: NACA 0012; M_∞= 0.8; α = 1.25°.

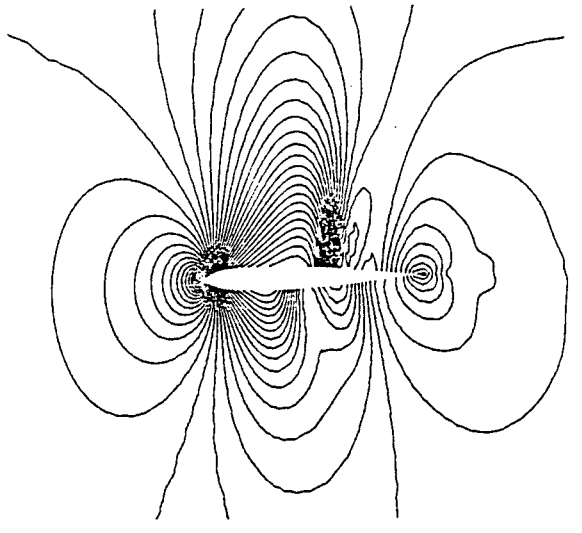

Fig.25 Whitfield's method: isobars for NACA 0012; M_∞= 0.8; α = 1.25°.

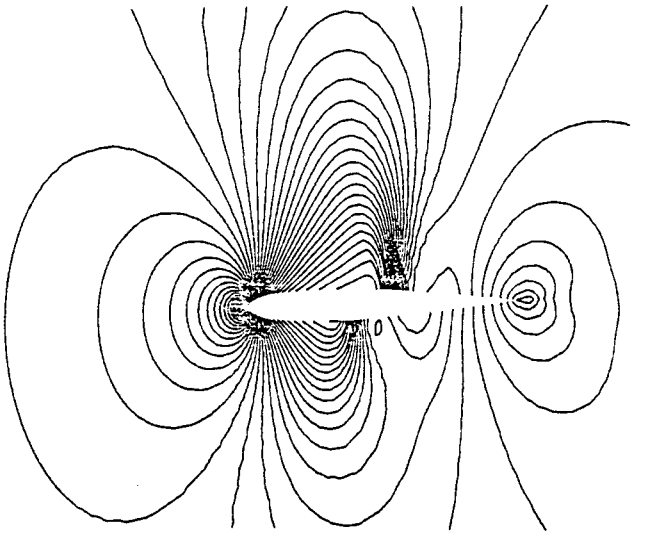

Fig.26 Steger-Warming method: isobars for NACA 0012; M_∞= 0.8; α = 1.25°.

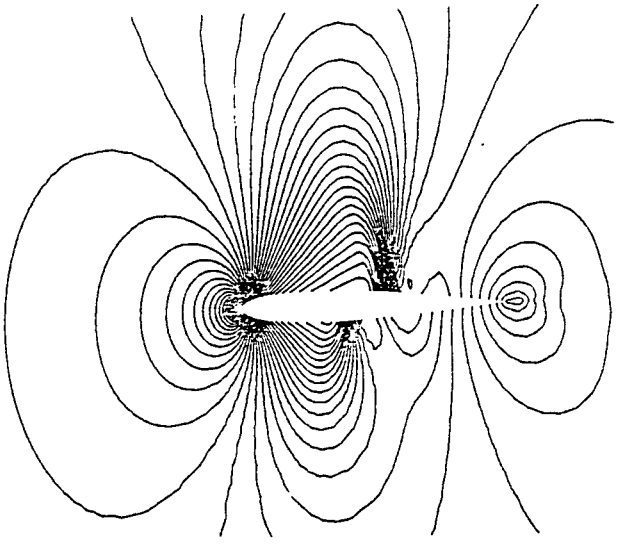

Fig.27 Deese's method: isobars for NACA 0012; M_∞= 0.8; α = 1.25°.

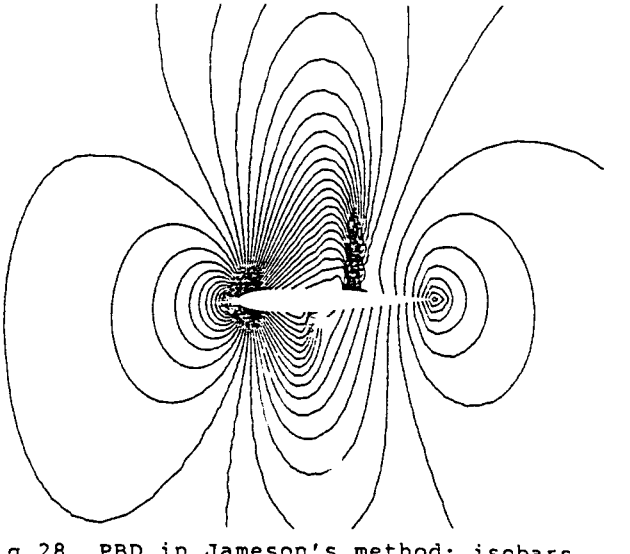

Fig.28 PBD in Jameson's method: isobars for NACA 0012; M_∞= 0.8; α = 1.25°.

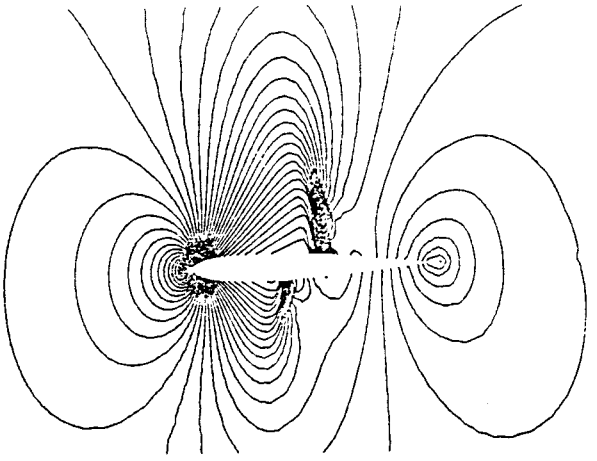

Fig.29 Van Leer's method: isobars for NACA 0012; $M_\infty = 0.8$; $\alpha = 1.25°$.

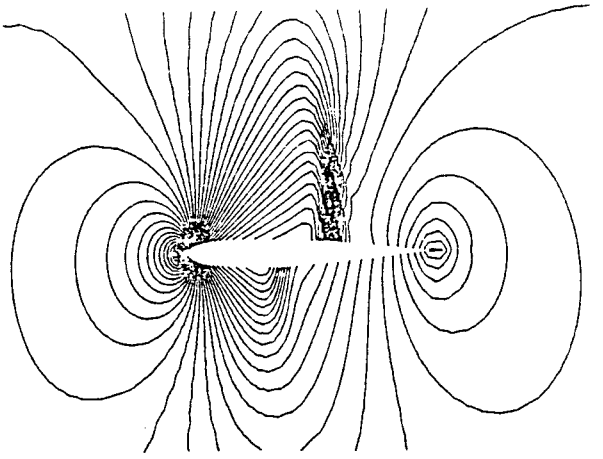

Fig.30 Original Jameson's method: isobars for NACA 0012; $M_\infty = 0.8$; $\alpha = 1.25°$.

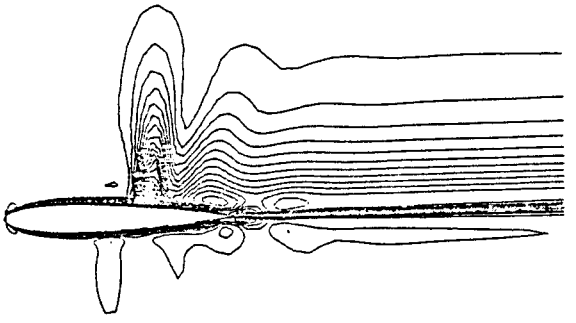

Fig.31 Whitfield's method: total pressure loss for NACA 0012; $M_\infty = 0.8$; $\alpha = 1.25°$.

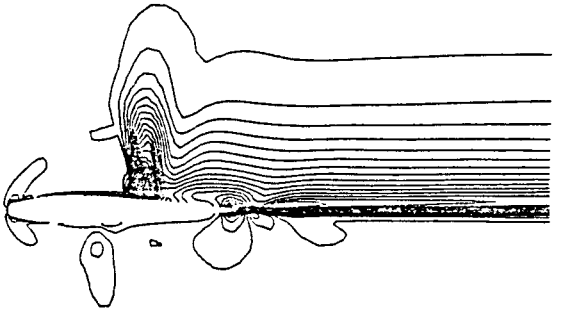

Fig.32 Steger-Warming method: total pressure loss for NACA 0012; $M_\infty = 0.8$; $\alpha = 1.25°$.

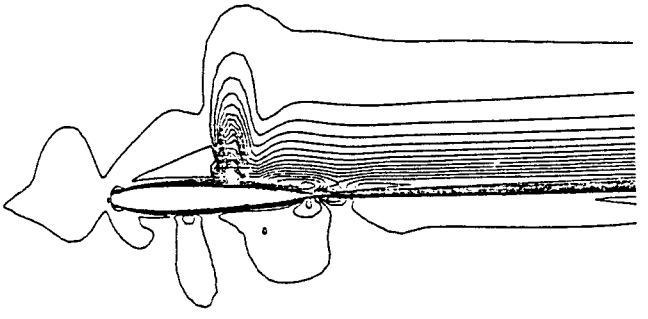

Fig.33 Deese's method: total pressure loss for NACA 0012; $M_\infty = 0.8$; $\alpha = 1.25°$.

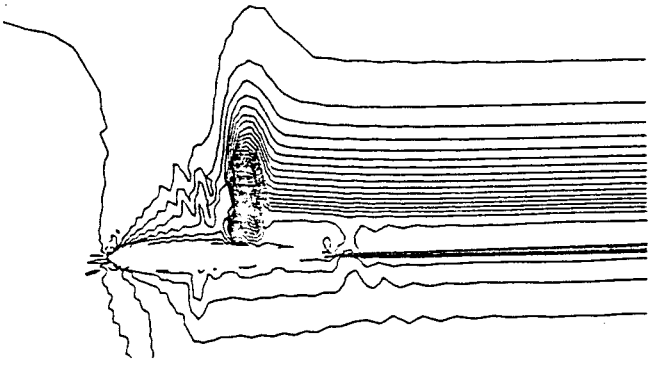

Fig.34 PBD method: total pressure loss for NACA 0012; $M_\infty = 0.8$; $\alpha = 1.25°$.

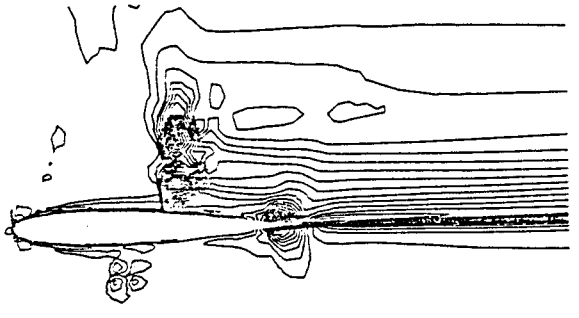

Fig.35 Van Leer's method: total pressure loss for NACA 0012; $M_\infty = 0.8$; $\alpha = 1.25°$.

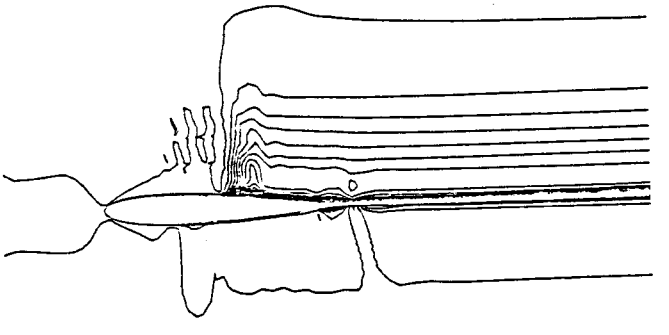

Fig.36 Jameson's method: total pressure loss for NACA 0012; $M_\infty = 0.8$; $\alpha = 1.25°$.